

In-situ observation of solidification behaviors of Fe-Mn-Cr-Ni-Si alloy during TIG melt-run welding using synchrotron radiation X-ray

Tomoya Nagira ^{a,*}, Houichi Kitano ^a, Takashi Kimura ^a, Fumiyoshi Yoshinaka ^a, Susumu Takamori ^a, Takahiro Sawaguchi ^a, Takayuki Yamashita ^b, Yasuhiro Aoki ^b, Hidetoshi Fujii ^b, Akihisa Takeuchi ^c, Masayuki Uesugi ^c

^a National Institute for Materials Science, 1-2-1, Sengen, Tsukuba, Ibaraki, 305-0047, Japan

^b Joining and Welding Research Institute, Osaka University, 11-1 Mihogaoka, Ibaraki, Osaka, 567-0047, Japan

^c Japan Synchrotron Radiation Research Institute, 1-1-1, Kouto, Sayo-cho, Sayo-gun, Hyogo, 679-5198, Japan

Abstract

The solidification behaviors, including the solidification cracking and solidification mode of the Fe-Mn-Cr-Ni-Si alloys at the weld bead during tungsten inert gas (TIG) melt-run welding, were examined by time-resolved in-situ observations using synchrotron radiation X-ray imaging and X-ray diffraction. The dynamics of initiation and propagation of solidification cracking at the weld bead could be observed at the dendrite scale. For the specimen solidified in the austenite mode at a welding speed of 10 mm/s, solidification cracking with a zigzag interface developed via the coalescence of many small pores at the centerline, where the columnar dendrite tips impinged. Quantitative image analysis indicated that the local tensile strain was highly localized at the centerline, and the critical local tensile strain for the initiation of solidification cracking was approximately 0.04. For the specimen solidifying in the ferrite-austenite mode at the welding speed of 10 mm/s, the centerline solidification cracking was suppressed by the formation of many equiaxed γ -Fe dendrites ahead of the growing columnar δ -Fe dendrites. Grain refinement at the centerline can be achieved at a welding speed of more than 7 mm/s without requiring inoculants.

Keywords: in-situ observation, solidification behaviors, solidification cracking, Fe-Mn-Cr-Ni-Si alloy, melt-run welding

*Corresponding author: Tel: +81-29-859-2408

E-mail: NAGIRA.Tomoya@nims.go.jp (T. Nagira)

1. Introduction

Recently, Fe-Mn-Cr-Ni-Si alloys with a high plastic fatigue life have been developed for application as seismic steel dampers in tower building [1,2]. A damper using an Fe-15Mn-10Cr-8Ni-4Si alloy as a core plate exhibited a fatigue life ten times longer than that of conventional steels [3]. However, the joining process was restricted to the mechanical joining technique using a bolt and nut owing to its high susceptibility to solidification cracking, which originates from austenite (A) mode solidification. To overcome this problem, the solidification mode from A to ferrite-austenite (FA) was changed by controlling the Cr/Ni equivalent ratio without degrading the plastic fatigue life [4]. The primary ferrite phase is known to contribute to the improvement in the solidification cracking susceptibility of austenitic stainless steel [5–7] because the lacy/skeletal ferrite and discontinuous liquid film provide crack resistance. However, the transformation from all ferrite phases to the austenite phase occurs during the cooling process of the Fe-Mn-Cr-Ni-Si alloy [4]. The observation of a solidified specimen consisting of the full austenite phase makes it difficult to examine the effect of the ferrite phase on solidification cracking. Meanwhile, in-situ observation of solidification behavior is the most direct approach to clarify the mechanism for preventing solidification cracking.

Researchers have examined the solidification behavior and phase transformations of certain steels during welding using synchrotron radiation X-ray diffraction [8–11]. Mirihanage et al. achieved in-situ time-resolved observations of rapid solidification behaviors, including grain growth and rotation, in austenitic steels during spot welding at an extremely high frame rate of 1 kHz [11]. Meanwhile, in-situ observation using synchrotron radiation X-ray imaging and a high-speed camera, which can be visually recognized, is more effective for understanding dynamic phenomena. These techniques have been applied to various solidification behaviors during welding such as weld pools [12], bubbles [13], porosity [13], and solidification cracking [14–19]. Some studies have demonstrated the strain distribution during the welding process and the critical strain for solidification cracking using quantitative image analysis of video sequences [17,19]. However, dendrite-scale microstructural evolution, such as dendrite growth, dendrite competition, and the relationship between the porosity/crack and dendrite microstructure during welding, are not fully understood because of the low spatial and time resolutions.

In a recent study, we developed a technique for the in-situ observation of dendrite growth and solidification cracking behaviors of the Fe-Mn-Cr-Ni-Si alloy at the weld crater during tungsten inert gas (TIG) spot welding using high-spatial resolution synchrotron radiation X-ray imaging [20,21]. This method enabled us to observe the

microstructural evolution in-situ at the dendrite scale during welding and directly obtain the critical strain for solidification cracking. Furthermore, phase transformation during solidification can be detected by combining X-ray diffraction with X-ray imaging. The Fe-Mn-Cr-Ni-Si alloy showed the unique FA mode where many equiaxed γ -Fe dendrites appeared in front of the growing columnar δ -Fe dendrites at the weld crater. In addition, the propagation of the solidification cracking was suppressed by the formation of many equiaxed γ -Fe dendrites. Therefore, the inhibition of solidification cracking is also expected at the weld bead as well as weld crater if a similar FA mode occurs during melt-run welding. However, in-situ observation of the weld bead for Fe alloys using synchrotron radiation X-ray imaging has been limited to dynamics of high-contrast images, such as the formation of small cracks and the propagation of solidification cracking [19].

In this study, we conducted an in-situ observation of the solidification behavior of an Fe-Mn-Cr-Ni-Si alloy at the weld bead during TIG melt-run welding using a developed technique that could observe the microstructural evolution at the dendrite-scale. The effect of the solidification mode on solidification cracking susceptibility was examined. A quantitative image analysis was conducted to obtain the local strain distribution during solidification cracking. The effect of welding speed on the solidification behavior in the FA mode was also examined. The solidification mechanism in the FA mode at a high welding speed is discussed in terms of thermal conditions and solute segregation in the liquid.

2. Experimental Procedures

Alloys with nominal compositions of Fe-15Mn-10Cr-8Ni-4Si and Fe-15Mn-11Cr-7.5Ni-4Si were used and are denoted as specimens X0 and X05, respectively. According to the phase diagram of the Fe-Mn-Cr-Ni-Si system calculated using Thermo-Calc software and the TCFE11 database, as shown in Fig. 1 [20], specimens X0 and X05 solidify in the A and FA modes, respectively. These alloys were fabricated in an induction furnace under Ar atmosphere, hot-forged at 1373K, and rolled into plates. Finally, heat treatment was conducted at 1273 K for 1 h, followed by quenching in water. The specimens were cut into dimensions of 50 mm length, 50 mm width and 0.2 mm thickness.

The in-situ experiments were performed at beamline 20XU of SPring-8, Japan. Fig. 2 shows a schematic of the experimental setup for the in-situ observations during TIG melt-run welding. The setup consisted of an X-ray imaging detector, X-ray flat panel sensor, TIG welding apparatus, specimen cell, high-speed camera, and slit placed along the X-ray beam path. The transmitted X-ray images were obtained at an X-ray energy of

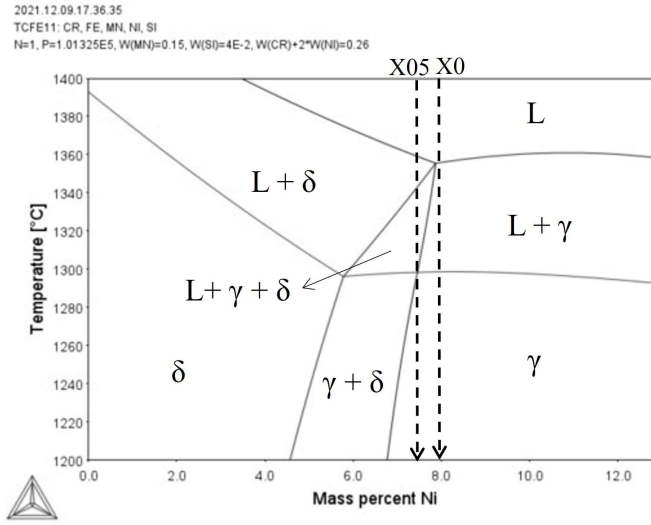


Fig. 1. Phase diagram of the Fe-Mn-Cr-Ni-Si system [20].

28 keV using an X-ray imaging detector consisting of a Complementary Metal Oxide Semiconductor (CMOS)-type high-speed camera, optical lens, and a phosphor screen of Ce-doped gadolinium-aluminum gallium garnet (GAGG) phosphor screen [22]. Two types of lenses were used to acquire the X-ray images. In the wide visual field lens, the observation area was 2.2×2.2 mm with a pixel size of $1.1 \mu\text{m}$. In the narrow visual field lens, the observation area was 1.0×1.0 mm with a pixel size of $0.49 \mu\text{m}$. For specimen X05, a narrow visual field lens was used to clearly observe the FA mode solidification. The frame rate and exposure time of each image were 50 fps and 20 ms, respectively. To suppress the X-ray phase contrast, the X-ray imaging detector was located at a distance of 30 cm from the specimen.

In-situ X-ray diffraction (XRD) and temperature measurements were performed using a flat panel sensor and a high-speed camera, respectively, simultaneously with in-situ X-ray imaging during TIG melt-run welding. XRD patterns were recorded at 60 fps with a pixel size of $200 \mu\text{m}$. Notably, the only XRD patterns within the weld bead were obtained using a silt. High-speed camera images were acquired at 250 fps, and the acquired images were converted to temperature images using the two-color method software (NAC Image Technology Inc., Thermias).

The specimens were fixed using a Cu plate and an Al backing plate with a hole for X-rays to pass through. The TIG torch was attached to the z-axis stage, which was moved upward/downward. TIG melt-run welding was performed by moving the TIG torch downward with an Ar shielding gas. The solidification behaviors of the two specimens were compared at a welding speed of 10 mm/s and a welding current of 8 A. To examine the effect of the welding speed on the solidification behavior of specimen X05, in-situ

experiments were conducted at four welding speeds of 5, 6, 7, and 8 mm/s at a welding current of 7 A. Notably, the full weld penetration was achieved under all welding conditions.

The solute distribution of the weld bead was determined using an electron probe microanalyzer (EPMA) for the specimen solidified in the FA mode. Specimen X05 was quenched using Ar gas after the in-situ experiment. The distribution of the local strain near the centerline of the weld bead during solidification cracking was evaluated using image processing techniques. Specifically, after the X-ray images were enhanced using bilateral filter processing [23] and adaptive histogram equalization processing [24], the displacement of each pixel, known as the optical flow, was calculated for each frame of the X-ray images using the TV-L1 method [25]. Subsequently, the obtained displacement fields are converted into strain fields. Typically, the Digital Image Correlation (DIC) method is used to calculate the strain field of time-series image data. However, when applied to the X-ray images obtained in this study, calculating the appropriate strain fields was challenging because of noise and brightness drift. Consequently, strain field calculations were performed using an optical flow evaluation method. The efficacy of this strain-field calculation method was also discussed by Hartmann et al. [26]. The strain at the solid/liquid interface, which corresponds to the fusion boundary, was defined as zero.

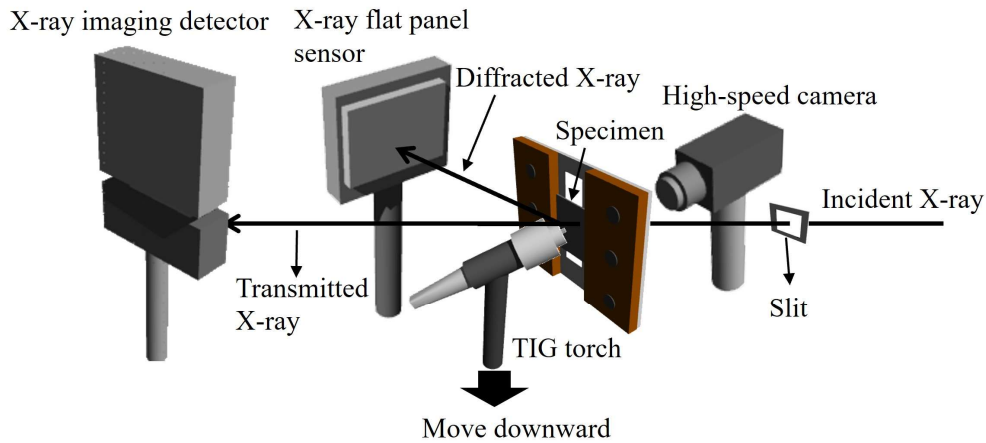


Fig. 2. Schematic of experimental setup for in-situ observation at the weld bead during TIG melt-run welding.

3. Results and Discussion

3.1 In-situ observation of solidification cracking for specimen X0

Fig. 3 shows the solidification sequence of specimen X0, which solidified in the A mode, at a welding speed of 10 mm/s. The complete time sequence of the solidification

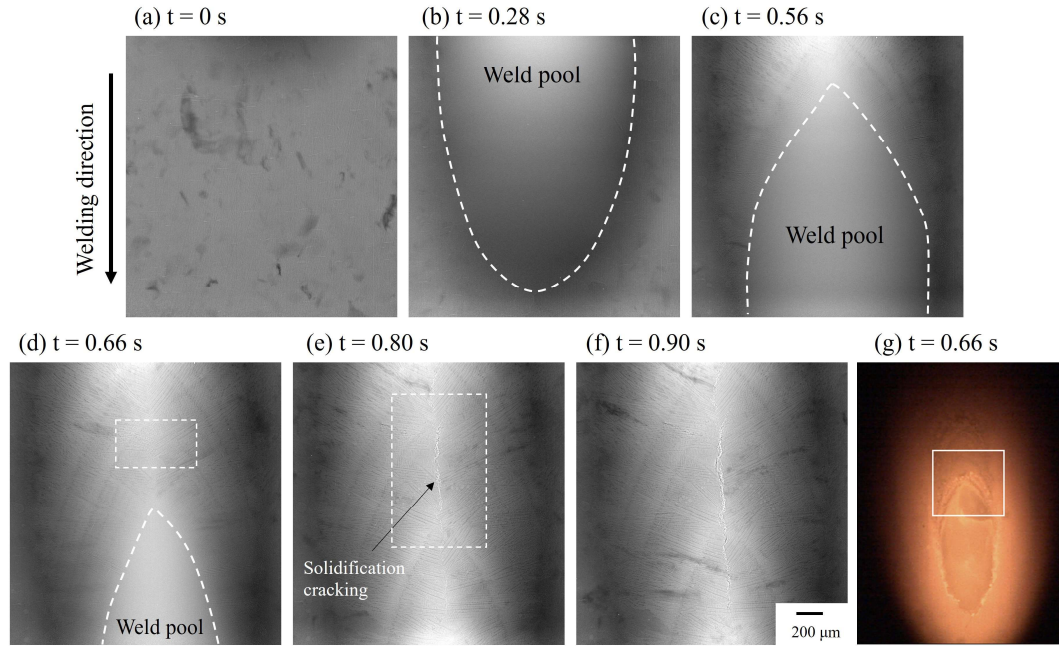


Fig. 3. (a–f) Solidification sequence of specimen X0 at the welding speed of 10 mm/s during TIG melt-run welding. White dotted lines denote the solid/liquid interface. (g) Camera image at 0.66 s; the white square corresponds to the X-ray radiograph of (d).

behavior is shown in Video 1. Fig. 3 (a) shows an X-ray radiograph before melting at $t = 0$ s. The TIG torch moved downward immediately after arc ignition. A weld pool with a teardrop-like shape was formed, as shown in Figs. 3(b) and (c), which was also identified in the camera image shown in Fig. 3(g), where the white square corresponds to the X-ray radiograph in Fig. 3(d). A teardrop shape is generally favored at high welding speeds [27]. As the weld pool moved downward further, columnar dendrites grew from both sides of the fusion boundary toward the centerline of the weld bead, as shown in Figs. 3(c) and (d). Subsequently, these columnar dendrites impinged on the centerline in a direction approximately parallel to the horizontal line. Solidification cracking initiated at the centerline, where the columnar dendrite tips impinged and propagated toward the welding direction, as shown in Figs. 3(e) and (f). Fig. 4 (a) shows the optical micrograph of the solidified specimen X0. The centerline solidification cracking was observed between the columnar grains, which was in agreement with the in-situ observation. The solidification cracking sequence in the white dotted square in Fig. 3(d) is shown in Fig. 5. Magnified images of the dotted squares in Figs. 5(c) and (d) are shown in Figs. 5(i) and (j), respectively. The growth of columnar dendrites was clearly observed at the weld bead, as shown in Figs. 5(a) and (b). The primary and secondary dendrite arm spacings at 0.58 s

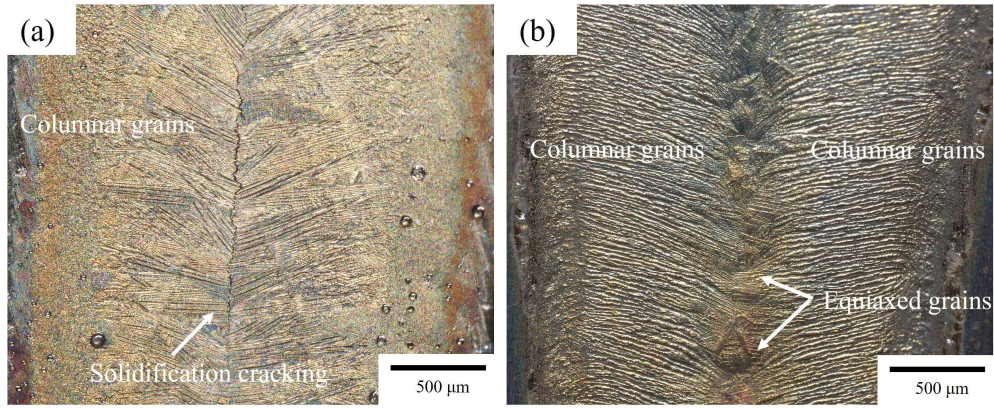


Fig. 4. Optical micrographs of solidified specimens (a) X0 and (b) X05 after the in-situ experiment.

were 50 μm and 8 μm , respectively. The columnar dendrites, which grew from both sides of the fusion boundary, impinged at 0.62 s at the centerline. The average growth velocity of the columnar dendrites immediately before the impingement of the dendrite tips was 6.2 mm/s. As the solidification proceeded, many small pores with a diameter of approximately 7 μm , as indicated by the black arrows in Fig. 5(c), appeared along the centerline at 0.72 s, indicating the initiation of solidification cracking. In this study, the

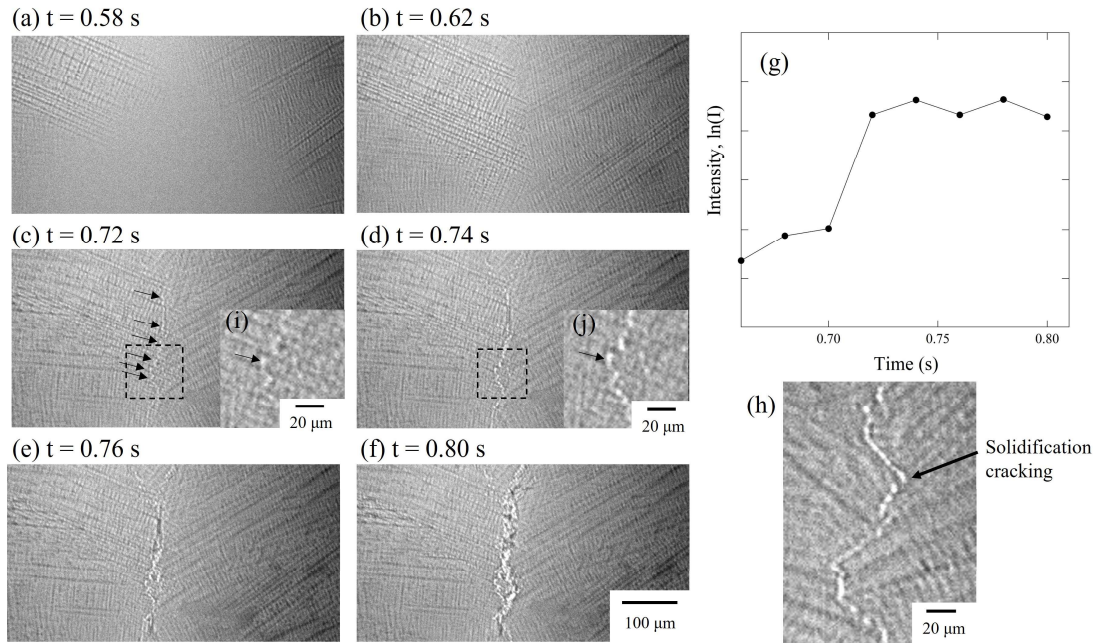


Fig. 5. (a–f) Evolution of solidification cracking of specimen X0 at welding speed of 10 mm/s during TIG melt-run welding. (g) Time dependence of X-ray intensity at the position, indicated by the black arrows in (i) and (j). (h) Example of solidification cracking at the centerline of the weld bead.

moment of pore formation was determined from the X-ray intensity and the X-ray imaging sequence. Fig. 5(g) shows the time dependence of the X-ray intensity at the position, as indicated by the black arrows in Figs. 5(i) and (j). The X-ray intensity increased remarkably at 0.72 s and remained unchanged after pore formation. The remarkable increase in the X-ray intensity indicates the opening of the pores because the attenuation of X-rays is negligibly small. Solidification cracking occurs via the rupture of the liquid film owing to the tensile force induced by the solidification shrinkage [28,29]. However, the liquid film could not be clearly resolved by X-ray imaging because the dendrite tips partially overlapped with those from the other side of the fusion boundary in the vicinity of the centerline. As the solidification proceeded further, the small cracks with a size of approximately 15 μm were formed via the coalescence of the small pores, as shown in Figs. 5(d) and (j). Finally, they evolved into large cracks with zigzag interfaces, as shown in Figs. 5(e) and (f). Solidification cracking was clearly distributed along the interface of the dendrite tips, as shown in Fig. 5(h). Our previous studies on the in-situ observation of the solidification behavior of Al-Cu alloys showed the evolution of solidification cracking, including the formation and coalescence of pores [18]. However, the relationship between the pores and microstructure has not been clarified because of the low spatial resolution. In this study, the morphology of solidification cracking was found to depend on the dendrite microstructure.

3.2 Strain distribution during the evolution of solidification cracking

Fig. 6 shows snapshots of the local strain distributions obtained by image analysis of specimen X0 at a welding speed of 10 mm/s during solidification cracking. The white dotted square in Fig. 3(e) represents the analysis region. As solidification proceeded, the high local strain in the direction perpendicular to the welding direction, which corresponded to the tensile strain, was localized at the centerline, where the columnar dendrites from both sides of the fusion boundary impinged (Fig. 3 and 5). When solidification cracking was initiated via the formation of many pores at the centerline (Fig. 5(c)), the localized local strain was approximately 0.04, as shown in Fig. 6(b). When the localized local strain at the centerline increased to approximately 0.06, as shown in Fig. 6(d), solidification cracking with a zigzag interface evolved via the coalescence of many pores (Fig. 5(f)). In our previous studies on the in-situ observation of solidification crack propagation for type 310S and 316L stainless steels during TIG welding [19], the distribution of local strain was examined using the DIC method. The critical local tensile strain for solidification cracking was 0.05. Therefore, solidification cracking occurred in the Fe-Mn-Cr-Ni-Si alloy at a local strain similar to that in conventional stainless steels.

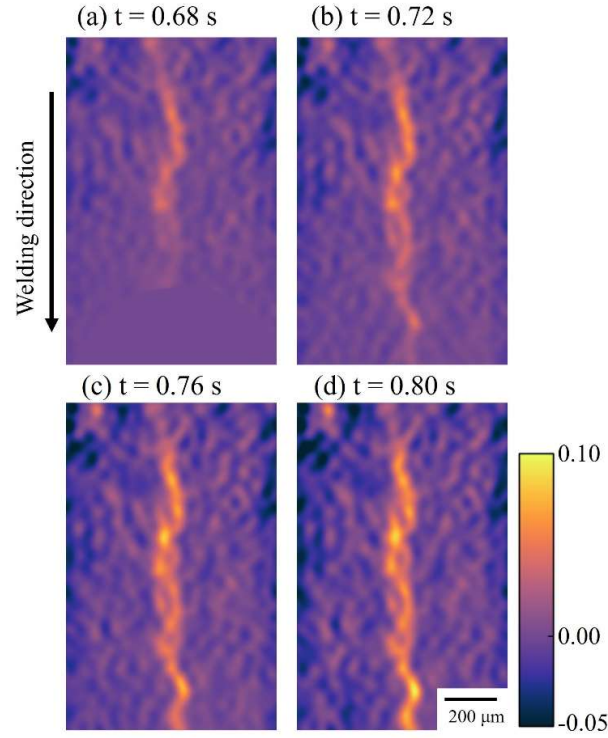


Fig. 6. Local strain distributions in the direction perpendicular to the welding direction at the centerline of the weld bead during solidification cracking.

3.3 In-situ observation of solidification behaviors for specimen X05

Fig. 7 shows the solidification sequence of specimen X05, which solidified in the FA mode at a welding speed of 10 mm/s. The complete time sequence of the solidification behavior is presented in Video 2. As in the case of specimen X0 (Fig. 3), the weld pool exhibited a teardrop-like shape owing to the high welding speed, as shown in Figs. 7(a) and (b). When the weld pool moved downward, the growth of the columnar dendrites from both sides of the fusion boundary toward the centerline of the weld bead occurred at $t = 0.30$ s, as shown in Fig. 7(b). A magnified image of the columnar dendrites in the dotted square in Fig. 7(b-1) is shown in Fig. 7(e). According to the XRD patterns in Fig. 8(a) and (b), the (110), (200), and (211) reflections of δ -Fe appeared from the liquid phase, corresponding to the halo pattern when the columnar dendrite grew at $t = 0.30$ s. The primary columnar dendrites were identified as the δ -Fe phase. When the columnar δ -Fe dendrite continued to grow, many equiaxed dendrites with darker contrast than that of the primary columnar dendrites appeared in front of the growing columnar δ -Fe dendrites in the vicinity of the centerline, as shown in Figs. 7(c) and (f) at $t = 0.36$ s. Furthermore, the

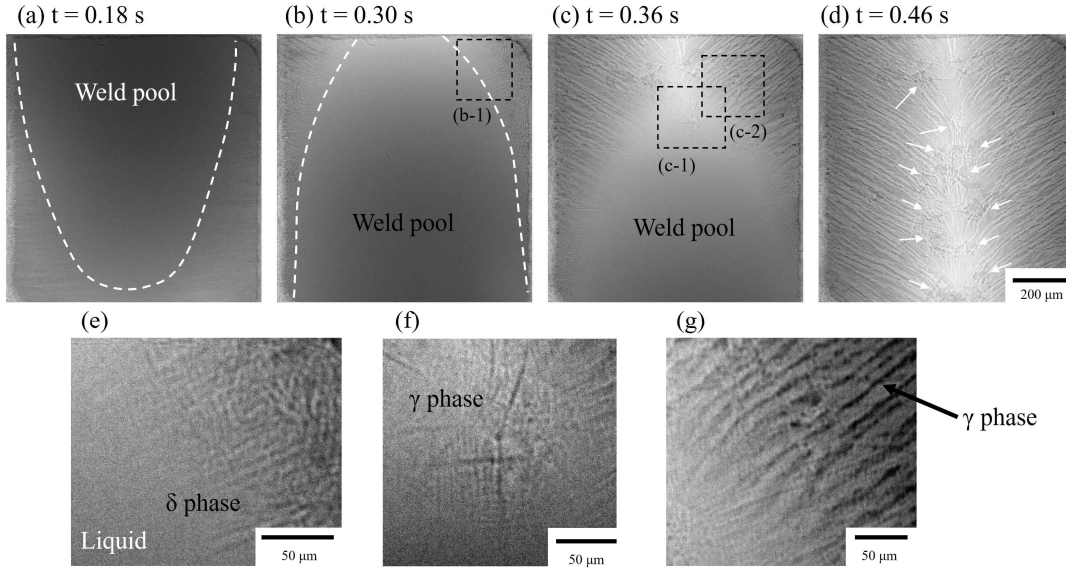


Fig. 7. (a–d) Solidification sequence of specimen X05 at welding speed of 10 mm/s during TIG melt-run welding. White dotted lines denote the solid/liquid interface. (e–g) Magnified images of the black dotted squares in (b-1), (c-1), and (c-2), respectively.

cellular crystals with darker contrast than that of the primary δ -Fe columnar dendrites grew independently in the interdendritic region between the columnar δ -Fe dendrites almost simultaneously with the formation of the equiaxed dendrites, as shown in Figs. 7 (c) and (g). The XRD patterns at 0.36 s showed that (111), (200), and (220) reflections of γ -Fe, as indicated by the white arrows, appeared, as shown in Fig. 8(c). Although the XRD patterns at 0.36 s could not be separated into the XRD patterns of equiaxed dendrites and those of the cellular crystals owing to the lack of time resolution, both of equiaxed dendrites and cellular crystals were identified as the γ -Fe phase likely because they have the lower transmitted X-ray intensity than that of the primary columnar δ -Fe dendrite. In principle, the γ -Fe phase shows the lower X-ray intensity than that of δ -Fe because of the higher density of γ -Fe phase than that of δ -Fe phase [30]. In the case of the conventional

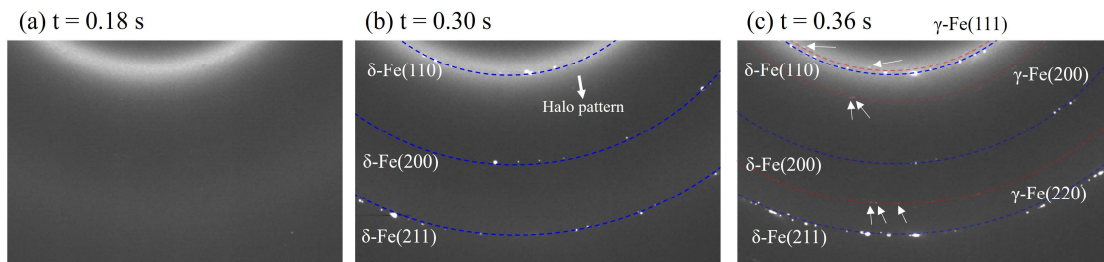


Fig. 8. XRD patterns of specimen X05 at (a) 0.18 s, (b) 0.30 s, and (c) 0.36 s.

FA mode, the cellular γ -Fe crystal is known to be formed independently through the divorced eutectic reaction in the interdendritic region between the columnar δ -Fe dendrites for the austenitic stainless steel [31,32]. However, the specimen X05 showed the formation of equiaxed γ -Fe dendrite as well as the cellular γ -Fe crystals in the interdendritic regions. This unique FA mode, where the equiaxed γ -Fe dendrite was formed in front of the columnar δ -Fe dendrite, was consistent with the solidification mode at the weld crater [20,21]. The solidification behavior was identified by the optical micrograph of the solidified specimen X05, as shown in Fig. 4(b). Many equiaxed grains were formed along the centerline between the columnar grains.

In contrast to specimen X0, no solidification cracking was observed in the centerline owing to the formation of many equiaxed grains, as indicated by the white arrows in Fig. 7(d), even at a high welding speed. Centerline solidification cracking can be suppressed by grain refinement, achieved by adding a grain refiner to an aluminum alloy [32–34], attributed to the distribution of strain induced by solidification shrinkage in the small grain boundaries [35]. The solidification cracking was not observed in the fully solidified specimen, as shown in Fig. 4(b).

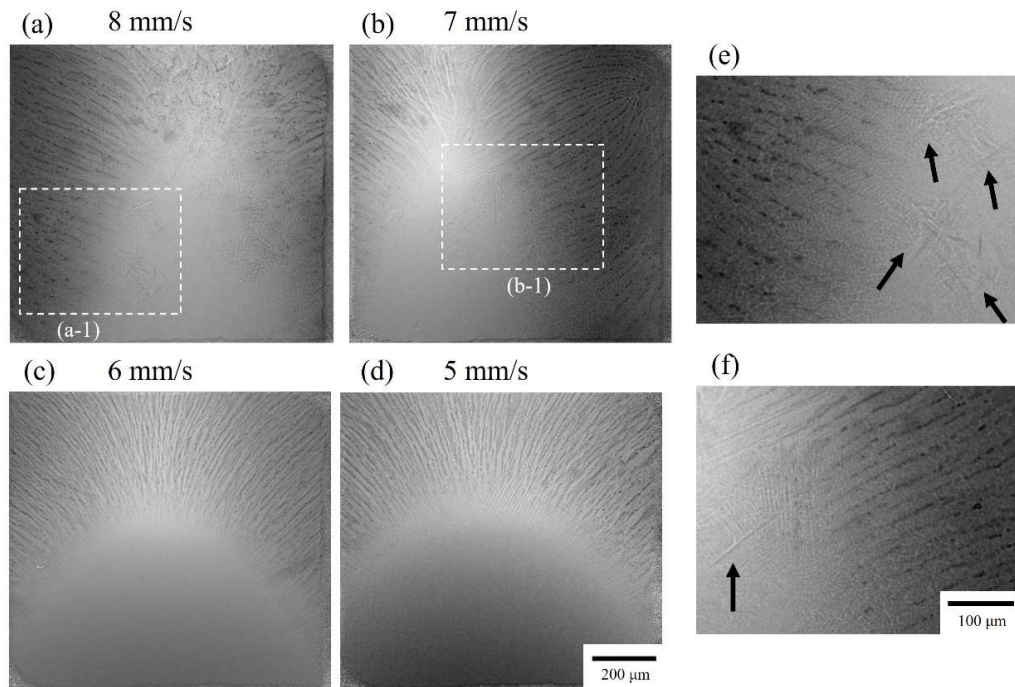


Fig. 9. X-ray radiographs of specimen X05 at welding speeds of (a) 8 mm/s, (b) 7 mm/s, (c) 6 mm/s, and (d) 5 mm/s. (e, f) Magnified images of the white dotted squares in (a-1) and (b-1), respectively. The black arrows denote the equiaxed dendrites.

3.4 Effect of the welding speed on the solidification behavior for specimen X05

Figs. 9(a-d) show the X-ray radiographs of specimen X05 at welding speeds of 8, 7, 6, and 5 mm/s, respectively. At welding speeds of 8 and 7 mm/s, the weld pool still exhibited a teardrop-like shape, as shown in Figs. 9(a) and (b). Magnified images of the white dotted squares in Figs. 9(a-1) and (b-1) are shown in Figs. 9(e) and (f), respectively. The formation of cellular crystals in the interdendritic regions and equiaxed dendrites in front of the growing columnar dendrites, as indicated by the black arrows in Figs. 9(e) and (f), respectively, was observed during solidification. They exhibited the same solidification behavior as those at a welding speed of 10 mm/s, as shown in Fig. 7. Meanwhile, at the lower welding speeds of 6 and 5 mm/s, the shape of the weld pool changed from a teardrop to an elliptical shape, as shown in Figs. 9(c) and (d). The weld pool is known to change from a teardrop to an elliptical or circular shape as the welding speed decreases [27]. No equiaxed dendrites were observed, and cellular crystals grew in the interdendritic regions between the columnar dendrites. These results indicate that the formation of equiaxed dendrites in front of the growing columnar dendrites depended on the welding speed.

Fig. 10 shows the solidification sequence of specimen X05 at a welding speed of 5 mm/s. The complete time sequence of the solidification behavior is presented in Video 3. As mentioned above, the weld pool exhibited an elliptical shape, as shown in Figs. 10(a) and (b), owing to its low welding speed. Magnified images of the black dotted squares in Figs. 10(b-1) and (c-1) are shown in Figs. 10(e) and (f), respectively. The primary columnar dendrites grew from the fusion boundary at 0.44 s, as shown in Fig. 10(e).

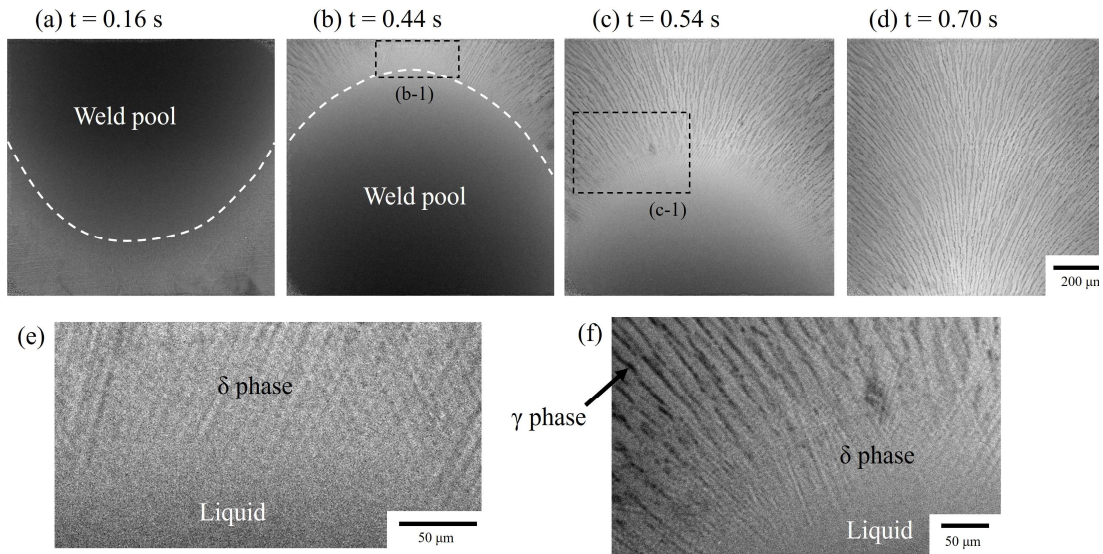


Fig. 10. (a–d) Solidification sequence of specimen X05 at welding speed of 5 mm/s. (e, f) Magnified images of the black dotted squares in (b-1) and (c-1), respectively.

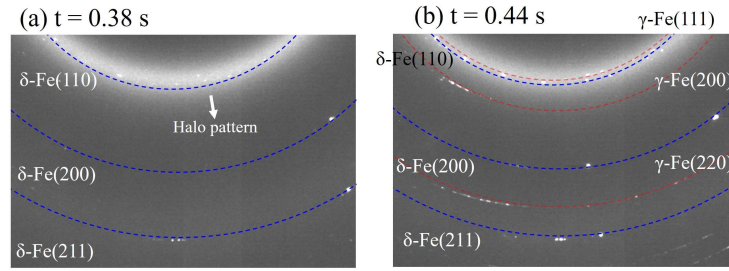


Fig. 11. XRD patterns of specimen X05 at (a) 0.38 s and (b) 0.44 s.

Subsequently, the growth of cellular crystal with darker image occurred in the interdendritic region between the primary columnar dendrites at 0.54 s, as shown in Figs. 10(c) and (f). Finally, the microstructure consisted of curved columnar grains, which is a conventional solidification structure for low welding speeds, as shown in Fig. 10(d). In general, columnar dendrites grow in the direction of the thermal gradient formed by the heat source. Therefore, the growth direction of the columnar dendrite continuously changes as the direction of the maximum thermal gradient changes from perpendicular to the weld surface to parallel to the welding direction during the movement of the heat source [36,37]. Figs. 11(a) and (b) show the XRD patterns of specimen X05 at 0.38 s and 0.44 s, respectively. When the primary columnar dendrites appeared at 0.38 s, the XRD pattern consisted of (110), (200) and (211) reflections of δ -Fe and the halo pattern. The primary columnar dendrites were identified as the δ -Fe phase. Then, as the cellular crystals were formed between the columnar δ -Fe dendrites, (111), (200) and (220) reflections of γ -Fe appeared at 0.44 s. Therefore, the specimen X05 at the low welding speed of 5 mm/s solidified in a conventional FA mode [31,32] where the cellular γ -Fe crystals were formed in the interdendritic regions between the primary columnar δ -Fe dendrites.

3.5 Possible mechanisms for the formation of equiaxed γ -Fe dendrites

As mentioned above, the specimen X05 showed the conventional FA mode solidification where the formation of the cellular γ -Fe crystals between the primary δ -Fe columnar dendrites occurred at the low welding speeds of 5 and 6 mm/s. When the welding speed increased up to 7 mm/s, the weld pool became the teardrop shape, and the columnar δ -Fe dendrites grew from both sides of the fusion boundary toward the centerline. As a result, the many equiaxed γ -Fe dendrites were formed in the melt ahead of the growing columnar δ -Fe dendrite in addition to the formation of the cellular γ -Fe crystals between the primary δ -Fe columnar dendrites. In general, nuclei in the melt ahead of the columnar grains are required to form equiaxed dendrites. However, at the present spatial and temporal resolutions, heterogeneous nucleation [38], nucleus formation via

dendrite fragmentation [39], and grain detachment [40] were not observed, thus making it important to examine the potential nuclei of equiaxed dendrites in future studies.

The columnar-to-equiaxed transition (CET) via the growth of nuclei requires favorable thermal condition [33,41–43]. It has been reported that the CET is determined by the ratio of the temperature gradient, G (K/mm) to the solidification velocity, R (mm/s) [33,41]. Generally, CET tends to occur at a low G/R ratio because of the high amount of constitutional undercooling. Figs. 12(a) and (b) show the time dependence of G , R , and G/R , respectively, at a welding speed of 10 mm/s. For comparison, the result of the weld crater for specimen X05 [20,21], where the formation of equiaxed dendrites also occurred ahead of the columnar dendrites, is plotted in Fig. 12(b). Examples of X-ray radiograph, camera image and temperature distribution are shown in Figs. 12(c), (d), and (e), respectively, which were used to calculate G and R . G at the solid/liquid interface was determined by comparing the X-ray radiograph with the temperature distribution. The R of the columnar dendrite was measured immediately before the equiaxed dendrite was

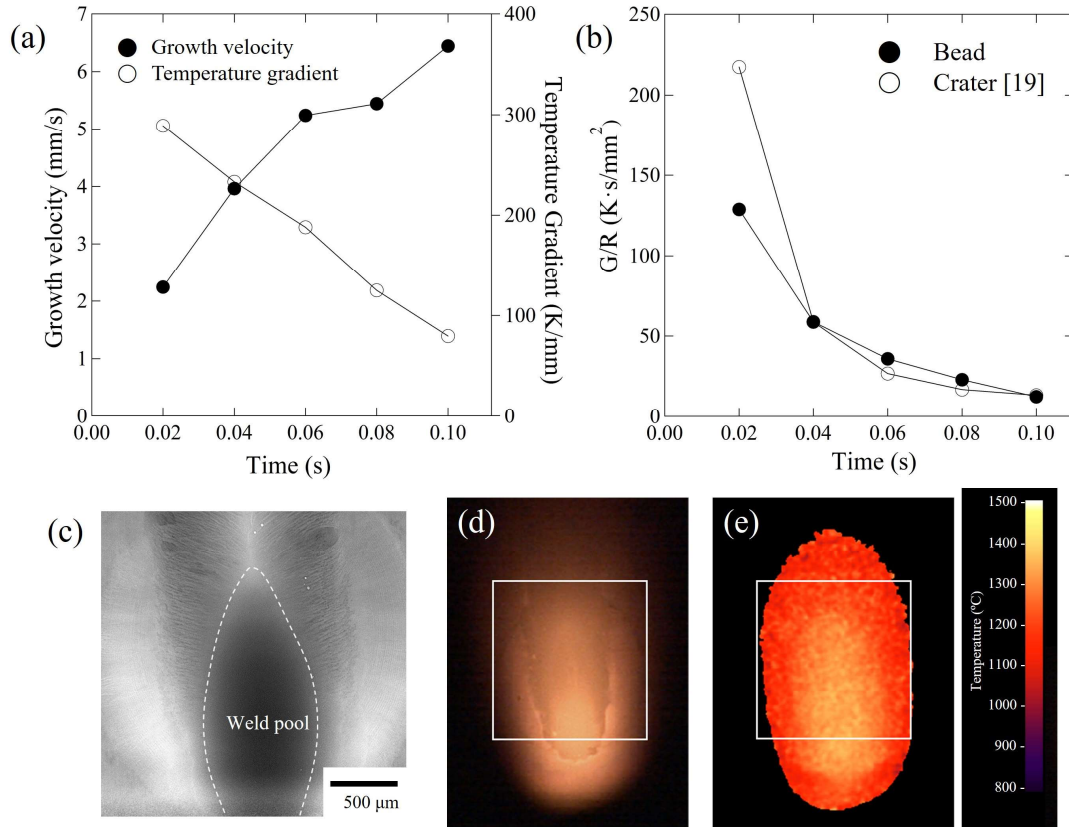


Fig. 12. Time dependences of (a) solidification velocity and temperature gradient at the weld bead (welding speed of 10 mm/s) and (b) G/R at the weld crater and bead for the specimen X05. (c) X-ray radiograph, (d) camera image, and (e) temperature distribution at 0.06 s; white squares correspond to the X-ray radiograph of (c).

formed. The G decreased from 290 K/mm to 80 K/mm whereas the R increased from 2.2 mm/s to 6.4 mm/s during the growth of columnar dendrites, as shown in Fig. 12(a). Consequently, G/R decreased remarkably to approximately one-tenth of its original value, as shown in Fig. 12(b). Similarly, the specimen X05 at the weld crater showed a remarkable decrease in G/R. Based on these results, CET likely occurred because of the significant decrease in G/R.

In our previous studies, solute enrichment in the liquid at the center of the weld pool occurred owing to solute rejection from the solid phase during the growth of columnar dendrites toward the center of the weld pool at the weld crater [20,21], likely causing a transition of the solidification mode during solidification. Lippold et al. showed that the solidification mode changed from the primary δ -Fe to the primary γ -Fe by the Ni enrichment in the liquid for the type 310/304 stainless steel during solidification [44]. At the weld bead, the solutes were also likely to be enriched in the melt of the centerline during the growth of columnar dendrites, which grew from both sides of the fusion boundary. To confirm the solute enrichment in the melt, EPMA analysis of specimen X05

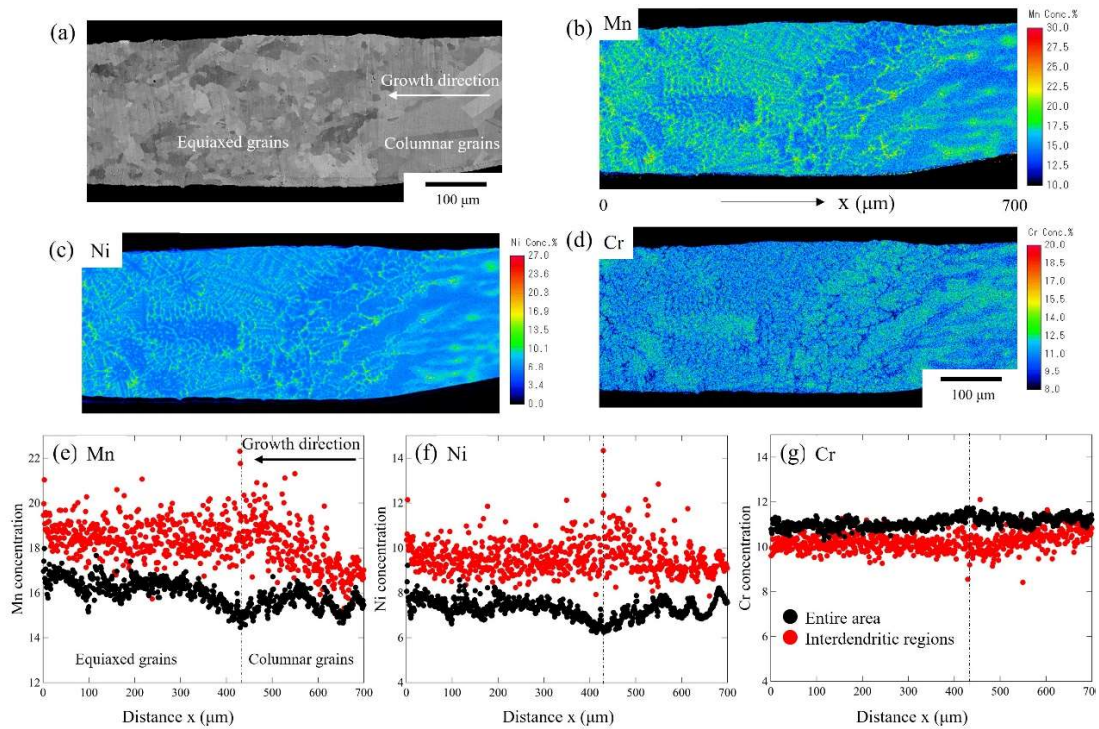


Fig. 13. (a) Microstructure for the transverse section of the quenched specimen X05 and EPMA mappings of (b) Mn, (c) Ni, and (d) Cr. Average concentrations of (e) Mn, (f) Ni, and (g) Cr for the entire area and interdendritic regions between the dendrite arms.

was conducted at a welding speed of 10 mm/s. Fig. 13(a) shows the microstructure of the quenched specimen X05, consisting of columnar and equiaxed grains on the transverse cross-section of the weld bead. Figs. 13(b), (c), and (d) show the EPMA mappings of Mn, Ni, and Cr, respectively. Notably, these distributions were likely influenced by the δ - γ solid-state transformation during the cooling because all δ -Fe transformed into the γ -Fe phase. Segregation of Mn and Ni occurred between the dendrite arms, whereas Cr was almost uniformly distributed throughout the weld bead. Figs. 13(e), (f), and (g) show the average concentrations of Mn, Ni, and Cr as functions of distance x for the entire area and the interdendritic regions between the dendrite arms. The Mn and Ni in the interdendritic regions gradually increased along the growth direction owing to the pile-up of solutes ahead of the growing solidification interface until equiaxed grains appeared and then remained almost unchanged in the region of equiaxed grains. The average concentrations of Mn and Ni in the interdendritic regions were approximately 13% and 31% higher, respectively, than those in the entire area within the equiaxed grain region. The average Cr concentration in the interdendritic regions was slightly lower than that over the entire area. These results indicate that the solutes Mn and Ni were highly enriched in the remaining liquid during solidification. According to our previous study on the Fe-Mn-Cr-Ni-Si alloys [4], when the Cr/Ni equivalent ratio was less than 1.51, the solidification mode changed from FA to A modes. Notably, the Cr/Ni equivalent ratio was calculated using the Peng's equations [45]. EPMA analysis showed that the Cr/Ni equivalent ratio decreased to approximately 1.29 for the interdendritic regions owing to an increase in the concentrations of Ni and Mn, leading to the change of the solidification mode from the primary δ -Fe to the primary γ -Fe. Therefore, γ -Fe could be preferentially nucleated in the remaining liquid during solidification by the solute enrichment of Mn and Ni. Based on these considerations, the remarkable decrease in G/R and the solute enrichment of Mn and Ni in the remaining liquid likely resulted in the formation of equiaxed γ -Fe dendrites in front of the growing columnar dendrites.

4. Conclusions

A technique for in-situ observation using synchrotron radiation X-ray imaging and X-ray diffraction was adopted to study the solidification behaviors, including the solidification cracking and solidification mode of the Fe-Mn-Cr-Ni-Si alloy at the weld bead during TIG melt-run welding. The effects of the solidification mode on solidification cracking and the welding speed on the solidification microstructure in the FA mode were examined. The mechanism of the equiaxed γ -Fe dendrite formation was discussed based on the thermal condition and the solute segregation in the liquid. The following

conclusions were drawn.

1. For specimen X0 solidified in the A mode at a welding speed of 10 mm/s, solidification cracking evolution at the weld bead could be observed at the dendrite scale. Solidification cracking was initiated by the formation of many small pores at the centerline where the columnar dendrite tips impinged. Image analysis showed that the localization of the high tensile strain occurred at the centerline, and the critical local strain of solidification cracking was approximately 0.04. The propagation of solidification cracking was caused by the coalescence of small pores. The zigzag interface of solidification cracking reflected the morphology of the columnar dendrite tips.
2. For specimen X05 solidifying in the FA mode at the welding speed of 10 mm/s, cellular γ -Fe crystals were formed independently in the interdendritic regions between the primary columnar δ -Fe dendrites. In addition, the formation of equiaxed γ -Fe dendrites occurred in the melt ahead of the growing columnar δ -Fe dendrites in the vicinity of the centerline, suppressing solidification cracking, even at high welding speeds.
3. The shape of the weld pool changed from teardrop to elliptical when the welding speed decreased below 6 mm/s. As a result, the specimen solidified in the conventional FA mode where the formation of the cellular γ -Fe crystals in the interdendritic regions between the primary columnar δ -Fe dendrites occurred without the formation of equiaxed dendrites.
4. G/R decreased significantly during columnar dendrite growth owing to the increase in R and decrease in G at a welding speed of 10 mm/s. Therefore, CET was expected to occur. In addition, the segregation of Mn and Ni occurred between the dendrite arms. This indicates the enrichment of their solutes in the remaining liquid during the growth of columnar dendrites, which likely caused the transition of the solidification mode from primary δ -Fe to primary γ -Fe.

Acknowledgements

The experiments were performed with the approval of the Japan Synchrotron Radiation Research Institute (JASRI) (Proposal Nos.2022A1096, 2022B1003, 2023A1131, and 2023B1201). This study was partially supported by the JSPS KAKENHI (grant number 23H01731).

Declaration of competing interest

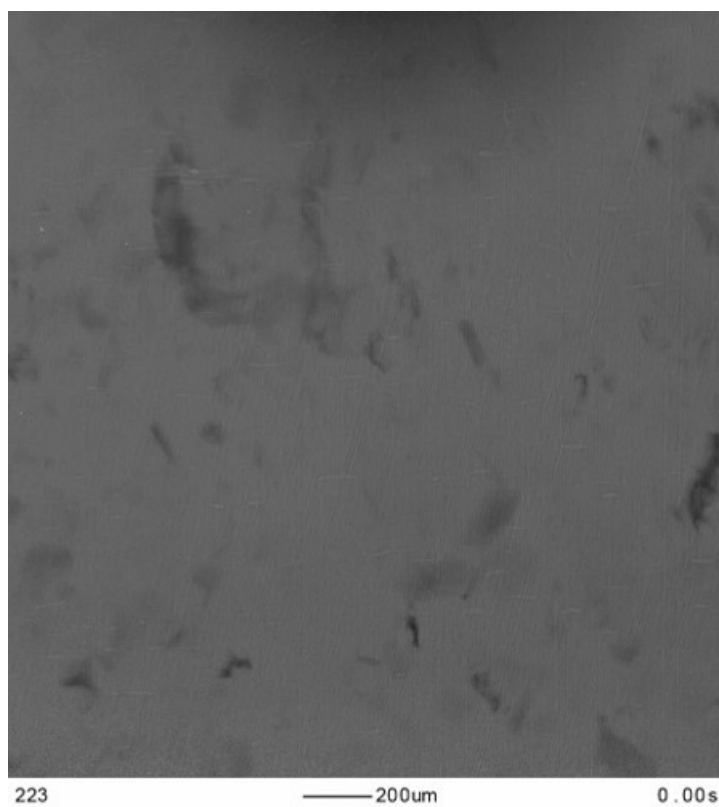
The authors declare that they have no competing financial interests or personal

relationships that may have influenced the work reported in this study.

CRedit authorship contribution statement

Tomoya Nagira: Conceptualization, Methodology, Investigation, Visualization, Writing- Original draft preparation. **Houichi Kitano:** Data curation, Software, Writing - Review & Editing. **Takashi Kimura:** Data curation, Software, Investigation. **Fumiyoshi Yoshinaka:** Investigation, Writing - Review & Editing. **Susumu Takamori:** Writing - Review & Editing. **Takahiro Sawaguchi:** Writing - Review & Editing. **Takayuki Yamashita:** Investigation, Writing - Review & Editing. **Yasuhiro Aoki:** Investigation, Writing - Review & Editing. **Hidetoshi Fujii:** Writing - Review & Editing. **Akihisa Takeuchi:** Investigation, Writing - Review & Editing. **Masayuki Uesugi:** Investigation, Writing - Review & Editing.

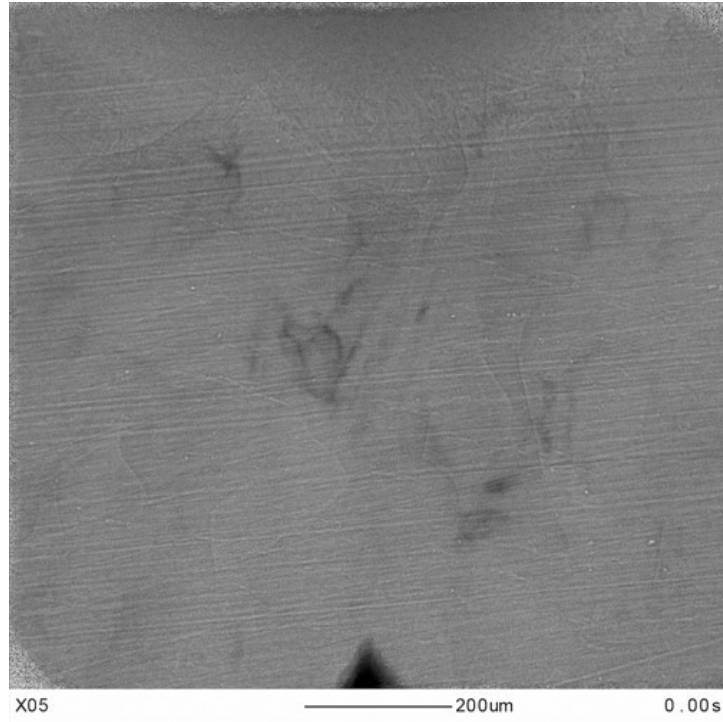
Supplementary materials



Video 1



Video 2



Video 3

References

- [1] T. Sawaguchi, I. Nikulin, K. Ogawa, K. Sekido, S. Takamori, T. Maruyama, Y. Chiba, A. Kushibe, Y. Inoue, K. Tsuzaki, Designing Fe-Mn-Si alloys with improved low-cycle fatigue lives, *Scr. Mater.* 99 (2015) 49–52. <https://doi.org/10.1016/j.scriptamat.2014.11.024>.
- [2] I. Nikulin, T. Sawaguchi, A. Kushibe, Y. Inoue, H. Otsuka, K. Tsuzaki, Effect of strain amplitude on the low-cycle fatigue behavior of a new Fe-15Mn-10Cr-8Ni-4Si seismic damping alloy, *Int. J. Fatigue*. 88 (2016) 132–141. <https://doi.org/10.1016/j.ijfatigue.2016.03.021>.
- [3] Y. Inoue, A. Kushibe, K. Umetani, Y. Mizushima, T. Sawaguchi, T. Nakamura, H. Otsuka, Y. Chiba, Fatigue-resistant Fe-Mn-Si-based alloy seismic dampers to counteract long-period ground motion, *Jap. Architect. Rev.* 4 (2021) 76–87. <https://doi.org/10.1002/2475-8876.12193>.
- [4] F. Yoshinaka, T. Sawaguchi, S. Takamori, T. Nakamura, G. Arakane, Y. Inoue, S. Motomura, A. Kushibe, Development of ferrous-based weldable seismic damping alloy with prolonged plastic fatigue life, *Scr. Mater.* 197 (2021) 113815. <https://doi.org/10.1016/j.scriptamat.2021.113815>.
- [5] T. Takalo, N. Suutala, T. Moisio, Austenitic solidification mode in austenitic stainless steel welds, *Metall. Trans. A* 10a. 10 (1979) 1173–1181. <https://doi.org/10.1007/BF02811663>.
- [6] P. Yu, K.J. Thompson, J. McCarthy, S. Kou, Microstructure evolution and solidification cracking in austenitic stainless steel welds, *Weld. J.* 97 (2018) 301–314. <https://doi.org/10.29391/2018.97.026>.
- [7] F. Matsuda, H. Nakagawa, I. Kato, Y. Murata, Solidification crack susceptibility in weld metals of duplex stainless steels, *Trans. JWRI*. 8 (1986) 105–112.
- [8] J.W. Elmer, J. Wong, T. Ressler, In-situ observations of phase transformations during solidification and cooling of austenitic stainless steel welds using time-resolved x-ray diffraction, *Scr. Mater.* 43 (2000) 751–757. [https://doi.org/10.1016/S1359-6462\(00\)00481-4](https://doi.org/10.1016/S1359-6462(00)00481-4).
- [9] S.S. Babu, J.W. Elmer, J.M. Vitek, S.A. David, Time-resolved X-ray diffraction investigation of primary weld solidification in Fe-C-Al-Mn steel welds, *Acta Mater.* 50 (2002) 4763–4781. [https://doi.org/10.1016/S1359-6454\(02\)00317-8](https://doi.org/10.1016/S1359-6454(02)00317-8).
- [10] H. Terasaki, Y. Komizo, M. Yonemura, T. Osuki, Time-resolved in-situ analysis of phase evolution for the directional solidification of carbon steel weld metal, *Metall. Mater. Trans. A*. 37 (2006) 1261–1266. <https://doi.org/10.1007/s11661-006-1077-8>.
- [11] W.U. Mirihanage, M. Di. Michiel, A. Reiten, L. Arnberg, H.B. Dong, R.H. Mathiesen,

- Time-resolved X-ray diffraction studies of solidification microstructure evolution in welding, *Acta Mater.* 68 (2014) 159–168. <https://doi.org/10.1016/j.actamat.2014.01.040>.
- [12] M. Miyagi, H. Wang, R. Yoshida, Y. Kawahito, H. Kawakami, T. Shoubu, Effect of alloy element on weld pool dynamics in laser welding of aluminum alloys, *Sci. Rep.* 8 (2018) 12944. <https://doi.org/10.1038/s41598-018-31350-4>.
- [13] L. Aucott, D. Huang, H.B. Dong, S.W. Wen, J.A. Marsden, A. Rack, A.C. Cocks, Initiation and growth kinetics of solidification cracking during welding of steel, *Sci. Rep.* 7 (2017) 40255. <https://doi.org/10.1038/srep40255>.
- [14] K. Shinozaki, M. Yamamoto, T. Tamura, P. Wen, Development of evaluation method for solidification cracking susceptibility of Inconel/SUS347 dissimilar laser weld metal by in-situ observation, *Mater. Sci. Forum.* 580–582 (2008) 49–52. <https://doi.org/10.4028/www.scientific.net/MSF.580-582.49>.
- [15] J.W. Aveson, G. Reinhart, B. Billia, H. Nguyen-Thi, N. Mangelinck-Noël, T.A. Lafford, C.A. Vie, J. Baruchel, H.J. Stone, Observation of the initiation and propagation of solidification cracks by means of in situ synchrotron X-ray radiography, *IOP Conf. S. Mater. Sci. Eng.* 33 (2012) 012040. <https://doi.org/10.1088/1757-899X/33/1/012040>.
- [16] K. Kadoi, A. Fujinaga, M. Yamamoto, K. Shinozaki, The effect of welding conditions on solidification cracking susceptibility of type 310S stainless steel during laser welding using an in-situ observation technique, *Weld. World.* 53 (2013) 383–390. <https://doi.org/10.1007/s40194-013-0023-9>.
- [17] N. Bakir, A. Gumenyuk, M. Rethmeier, Investigation of solidification cracking susceptibility during laser beam welding using an in-situ observation technique, *Sci. Tech. Weld. Join.* 23 (2018) 234–240. <https://doi.org/10.1080/13621718.2017.1367550>.
- [18] T. Nagira, D. Yamashita, M. Kamai, H. Liu, Y. Aoki, H. Fujii, K. Uesugi, A. Takeuchi, Time-resolved X-ray imaging of solidification cracking for Al-Cu alloy at the weld crater, *Mater. Charact.* 167 (2020) 110469. <https://doi.org/10.1016/j.matchar.2020.110469>.
- [19] T. Nagira, D. Yamashita, M. Kamai, H. Liu, Y. Aoki, K. Uesugi, A. Takeuchi, H. Fujii, In situ observation of solidification crack propagation for type 310S and 316L stainless steels during TIG welding using synchrotron X-ray imaging, *J. Mater. Sci.* 56 (2021) 10653–10663. <http://doi.org/10.1007/s10853-021-05969-0>.
- [20] T. Nagira, T. Nakamura, F. Yoshinaka, T. Sawaguchi, Y. Aoki, M. Kamai, H. Fujii, A. Takeuchi, M. Uesugi, Direct observation of solidification behaviors of Fe-Mn-Si

- alloys during arc spot welding using synchrotron X-ray, *Scr. Mater.* 216 (2022) 114743. <https://doi.org/10.1016/j.scriptamat.2022.114743>.
- [21] T. Nagira, T. Nakamura, T. Kimura, F. Yoshinaka, T. Sawaguchi, T. Yamashita, Y. Aoki, H. Fujii, Elucidation of solidification mode of Fe-Mn-Si alloy during TIG spot welding using synchrotron X-ray, *Q. J. Jpn. Weld. Soc.* 41 (2023) 1s–5s. <https://doi.org/10.2207/qjjws.41.1s>.
- [22] S. Goto, K. Takeshita, Y. Suzuki, H. Ohashi, Y. Asano, H. Kimura, T. Matsushita, N. Yagi, N. Isshiki, H. Yamazaki, Construction and commissioning of a 215-m-long beamline at SPring-8, *Nucl. Instrum. Method. A.* 467–468 (2001) 682–685. [https://doi.org/10.1016/S0168-9002\(01\)00445-4](https://doi.org/10.1016/S0168-9002(01)00445-4).
- [23] C. Tomasi, R. Manduchi, Bilateral Filtering for Gray and Color Images, 1998. pp. 839–846. <https://doi.org/10.1109/ICCV.1998.710815>.
- [24] K. Zuiderveld, Contrast limited adaptive histogram equalization, *graphics gems. IV* (1994) 474–485. <https://doi.org/10.1016/B978-0-12-336156-1.50061-6>.
- [25] J. Sánchez Pérez, E. Meinhardt-Llopis, G. Facciolo, TV-L1 Optical Flow Estimation, *Image Process. On Line.* 3 (2013) 137–150. <https://doi.org/10.5201/ipol.2013.26>.
- [26] C. Hartmann, J. Wang, D. Opristescu, W. Volk, Implementation and evolution of optical flow methods for two-dimensional deformation measurement in comparison to digital image correlation, *Opt. Lasers Eng.* 107 (2018) 127–141. <https://doi.org/10.1016/j.optlaseng.2018.03.021>.
- [27] S. Kou, Y. Le, Welding parameters and the grain structure of weld metal – A thermodynamic consideration, *Metall. Trans. A.* 19a (1988) 1075–1082. <https://doi.org/10.1007/BF02628392>.
- [28] M.C. Flemings, Behavior of metal alloys in the semisolid state, *Metall. Trans. A.* 22 (1991) 957–981. <https://doi.org/10.1007/BF02661090>.
- [29] G. Mathers, *The Welding of Aluminium and Its Alloys*, Woodhead Publishing, 2002. pp. 10–34. <https://doi.org/10.1533/9781855737631.10>.
- [30] T. Nishimura, K. Morishita, M. Yoshiya, T. Nagira, H. Yasuda, Time-resolved and In-situ observation of δ - γ transformation during unidirectional solidification in Fe-C alloys, *ISIJ Int.* 60 (2020) 930–938. <https://doi.org/10.2355/isijinternational.ISIJINT-2019-636>.
- [31] H. Inoue, T. Koseki, Solidification mechanism of austenitic stainless steels solidified with primary ferrite, *Acta Mater.* 124 (2017) 430–436. <https://doi.org/10.1016/j.actamat.2016.11.030>.
- [32] J.C. Villafuerte, H.W. Kerr, S.A. David, Mechanisms of equiaxed grain formation in ferritic stainless steel gas tungsten arc welds, *Mater. Sci. Eng. A* 194 (1995) 187–

191. [https://doi.org/10.1016/0921-5093\(94\)09656-2](https://doi.org/10.1016/0921-5093(94)09656-2).
- [33] G.D. Janaki Ram, T.K. Mitra, M.K. Raju, S. Sundaresan, Use of inoculants to refine weld solidification structure and improve weldability in type 2090 Al-Li alloy, *Mater. Sci. Eng. A* 276 (2000) 48–57. [https://doi.org/10.1016/S0921-5093\(99\)00515-8](https://doi.org/10.1016/S0921-5093(99)00515-8).
- [34] M.G. Mousavi, C.E. Cross, Ø. Grong, Effect of scandium and titanium-boron on grain refinement and hot cracking of aluminium alloy 7108, *Sci. Tech. Weld. Join.* 4 (1999) 381–388. <https://doi.org/10.1179/136217199101538030>.
- [35] J.A. Spittle, A.A. Cushway, Influence of superheat and grain structure on hot-tearing susceptibilities of Al-Cu alloy casting, *Met. Technol.* 10 (1983) 6-13. <https://doi.org/10.1179/030716983803291226>.
- [36] S. Kou, *Welding metallurgy*. 3rd ed., John Wiley and Sons, 2021.
- [37] J.C. Lippold, *Welding Metallurgy and Weldability*, John Wiley and Sons, 2015.
- [38] S. Kou, Y. Le, Nucleation mechanisms and grain refining of weld metal. *Weld. J.* 65 (1986) 305–313.
- [39] T. Koseki, Solidification and solidification structure control of solid metals, *Weld. Int.* 16 (2002) 347–365. <https://doi.org/10.1080/09507110209549544>.
- [40] B.P Pearce, H.W. Kerr, Grain refinement in magnetically stirred GTA welds of aluminum alloys, *Metall. Trans. B.* 12b (1981) 479–489. <https://doi.org/10.1007/BF02654317>.
- [41] G.D. Janaki Ram, T.K. Mitra, M.K. Raju, S. Sundaresan, Use of inoculants to refine weld solidification structure and improve weldability in type 2090 Al-Li alloy, *Mater. Sci. Eng. A.* 276 (2000) 48–57. [https://doi.org/10.1016/S0921-5093\(99\)00515-8](https://doi.org/10.1016/S0921-5093(99)00515-8).
- [42] J.A. Spittle, Columnar to equiaxed grain transition in as solidified alloys, *Int. Mater. Rev.* 51 (2006) 247–269. <https://doi.org/10.1179/174328006X102493>.
- [43] W. Kurz, C. Bezençon, M. Gäumann, Columnar to equiaxed transition in solidification processing, *Sci. Technol. Adv. Mater.* 2 (2001) 185–191. [https://doi.org/10.1016/S1468-6996\(01\)00047-X](https://doi.org/10.1016/S1468-6996(01)00047-X).
- [44] J.C. Lippold, W.F. Savage, Solidification of austenitic stainless steel weldments: Part 2 - The effect of alloy composition on ferrite morphology, *Weld. J.* 59 (1980) 48s-58s.
- [45] H. Peng, Y. Wen, Y. Du, J. Chen, Q. Yang, A New set of Creq and Nieq equations for predicting solidification modes of cast austenitic Fe-Mn-Si-Cr-Mo shape memory alloys, *Metall. Mater. Trans. B.* 45 (2014) 6–11. <https://doi.org/10.1007/s11663-013-0005-8>.